Remote Sensing of Radiative and Microphysical Properties of Clouds during TC^4: Results from MAS, MASTER, MODIS, and MISR

MICHAEL D. KING,[1,2] STEVEN PLATNICK,[2] GALINA WIND,[3,2]
G. THOMAS ARNOLD,[3,2] AND ROSEANNE T. DOMINGUEZ[4]

Short title: Remote Sensing of Cloud Properties during TC^4

Journal of Geophysical Research - Atmospheres
(Manuscript received 26 September 2009)

[1] Laboratory for Atmospheric and Space Physics, University of Colorado, Boulder, Colorado.
[2] Earth Sciences Division, NASA Goddard Space Flight Center, Greenbelt, Maryland.
[3] Science Systems and Applications, Inc., Lanham, Maryland.
[4] Airborne Science & Technology Lab, NASA Ames Research Center, Moffett Field, California.

ABSTRACT

The Moderate Resolution Imaging Spectroradiometer (MODIS) Airborne Simulator (MAS) and MODIS/Airborne Spaceborne Thermal Emission and Reflection Radiometer (ASTER) Airborne Simulator (MASTER) were used to obtain measurements of the bidirectional reflectance and brightness temperature of clouds at 50 discrete wavelengths between 0.47 and 14.2 μm (12.9 μm for MASTER). These observations were obtained from the NASA ER-2 aircraft as part of the Tropical Composition, Cloud and Climate Coupling (TC^4) experiment conducted over Central America and surrounding Pacific and Atlantic Oceans between 17 July and 8 August 2007. Multispectral images in eleven distinct bands were used to derive a confidence in clear sky (or alternatively the probability of cloud) over land and ocean ecosystems. Based on the results of individual tests run as part of the cloud mask, an algorithm was developed to estimate the phase of the clouds (liquid water, ice, or undetermined phase). The cloud optical thickness and effective radius were derived for both liquid water and ice clouds that were detected during each flight, using a nearly identical algorithm to that implemented operationally to process MODIS cloud data from the Aqua and Terra satellites (Collection 5).

This analysis shows that the cloud mask developed for operational use on MODIS, and tested using MAS and MASTER data in TC^4, is quite capable of distinguishing both liquid water and ice clouds during daytime conditions over both land and ocean. The cloud optical thickness and effective radius retrievals use five distinct bands of the MAS (or MASTER), and these results were compared with nearly simultaneous retrievals of marine liquid water clouds from MODIS on the Terra spacecraft. Finally, this MODIS-based algorithm was adapted to Multiangle Imaging SpectroRadiometer (MISR) data to infer the cloud optical thickness of liquid water clouds from MISR. Results of this analysis are compared and contrasted.

1. Introduction

The temporal and spatial distribution of cloud radiative properties is crucial to the understanding of the radiative forcing of climate. High quality multispectral imagery acquired from satellite platforms is the most efficient and reliable means of fulfilling these global observational requirements, provided the retrievals are valid with known uncertainties. Between 17 July and 8 August 2007, the National Aeronautics and Space Administration (NASA) ER-2 high altitude research aircraft conducted 11 research flights over Central America and the neighboring eastern Pacific Ocean and Caribbean Sea as part of the TC^4 experiment [*Toon et al.*, 2010], part of whose focus was to help validate satellite retrievals of cloud optical properties. The NASA ER-2 aircraft was equipped with nine sensors, among which the MODIS Airborne Simulator (MAS) [*King et al.*, 1996] was designed to obtain measurements that simulate those obtained from MODIS, a 36-band spectroradiometer launched aboard the Earth Observing System (EOS) Terra [*King and Herring*, 2000] and Aqua [*Parkinson*, 2003] spacecraft. Due to technical problems with the MAS instrument part way through the experiment, the MAS was swapped out with the MODIS/ASTER Airborne Simulator (MASTER) [*Hook et al.*, 2001], which is similar in design to MAS except that it has more spectral bands of overlap with the ASTER (Advanced Spaceborne Thermal Emission and Reflectance Radiometer) instrument on Terra but lacks so-called CO_2 slicing bands bands in the 13-14 μm spectral region used to derive cloud top properties of middle and upper layer clouds.

The strategy for TC^4 included spaceborne remote sensing, high altitude remote sensing (NASA ER-2 at ~20 km), high altitude *in situ* measurements of cloud microphysics and atmospheric composition (NASA WB-57F), and medium altitude profiles and structure of cloud particles, radiation, and atmospheric composition (NASA DC-8). In addition, there were numerous ground-based observing facilities (primarily radar), and modeling studies. TC^4 took advantage of, and overlapped with, many NASA research satellites. Due to increasing convective activity over the central Costa Rica highlands in the afternoon, the vast majority of flights of the ER-2 landed shortly after noon, and hence the opportunities for coordination with Aqua and other spacecraft in the afternoon A-train constellation was minimal. Many flight opportunities included coordination with Terra (and TRMM) during late morning time periods. The ER-2 was based in San Jose, Costa Rica and deployed primarily over the eastern Pacific off the coasts of Central America and South America, with only one foray into the Caribbean to track a Saharan aerosol layer.

The main role of the ER-2 included: (i) simulating a wide variety of instruments currently operating on NASA Earth-observing satellites, (ii) collecting MAS (and MASTER) data to verify the MODIS cloud mask, thermodynamic phase, and cloud radiative and microphysical properties in the tropics during summer daytime conditions, (iii) determining the radiative energy budget of clouds, and (iv) extending the period of time when satellite remote sensing data are available for monitoring the tropical tropopause transition layer (TTL) using the wide array of remote sensing 'simulators' onboard the aircraft.

We begin by describing the approach and algorithms used to detect clouds during daytime conditions from MAS and MASTER. This represents a subset of all conditions and bands used to process global satellite data using MODIS, but is representative of land and ocean surfaces encountered during TC^4. Given the results from the cloud mask, we have developed an algorithm, currently implemented in the MODIS global processing system, to estimate the thermodynamic phase of clouds [*Platnick et al.*, 2003]. Important and significant refinements have been incorporated into MODIS Collection 5 processing and implemented in MAS and MASTER analysis, outlined in some detail here. Finally, we have retrieved cloud optical thickness and effective radius for the "cloudy" scenes identified from the MAS and MASTER during TC^4. Results obtained from the ER-2 on 29 July and 6 August 2007 during TC^4 are presented to illustrate the results of applying these cloud tests, thermodynamic phase decisions, and cloud microphysical retrievals to a wide range of conditions. The flights were selected due to the close coordination with Terra overpasses containing both MODIS and MISR instruments, where the MODIS cloud retrieval algorithms were adapted to MISR data for the first time. Comparison of these results helps to assess the accuracy that can be expected from global analysis of cloud optical properties from MODIS during the daytime.

2. Instrumentation

The MAS is a cross-track scanning spectrometer that measures reflected solar and emitted thermal radiation in 50 narrowband channels. For the TC^4 deployment, the configuration of the MAS contained channels between 0.47 and 14.2 μm. Flown aboard the NASA ER-2 aircraft, the MAS is a cross-track scanner with the maximum scan angle extending 43° on either side of nadir (86° full swath aperture). At a nominal ER-2 altitude of 20 km, this yields a swath width of 37.2 km at the earth's surface, centered on the aircraft ground track, with a total of 716 earth-viewing pixels acquired per scan. With each pixel having a 2.5 mrad instantaneous field of view, the ground spatial resolution is 50 m at nadir from the nominal aircraft altitude.

Table 1 summarizes the band center and bandwidth characteristics as well as main purpose of each MAS band used for cloud retrievals during TC^4. Some of these bands are used to discriminate clouds from clear sky (cloud mask), whereas others are used to derive the thermodynamic phase (liquid water or ice) and optical, physical, and microphysical properties of clouds. The bands used for these purposes are identified in Table 1, and a description of the phase algorithm used in this investigation is presented in section 3. Radiometric calibration of the shortwave (<2.5 μm) channels was obtained by observing laboratory standard integrating sphere sources on the ground prior to this experiment. Calibration of the infrared channels was performed by viewing two onboard blackbody sources once every scan, and the calibration was applied scan by scan. We also compared radiometric reflectance measurements from the MAS with a 210 km section of collocated MODIS observations obtained by the Aqua spacecraft on both 28 June and 9 July, just prior to deployment to Costa Rica. Based on these observations, we made calibration adjustments to the MAS spectrometer ranging from 7% at 0.66 μm to 13% at 2.13 μm, since the MAS consistently measured larger radiances than MODIS in this spectral range. A detailed description of the optical, mechanical, electronics and data acquisition system design of the MAS can be found in *King et al.* [1996].

Due to difficulty that developed in aligning the optical encoder light bulb with the encoder wheel, necessary to generate the sync pulse timing and control the scan motor speed, the MAS acquired data for only 3 research flights between 17 and 21 July for a total of 13.5 hours of research data. As a consequence, the remaining flights were obtained using a closely related MASTER instrument [*Hook et al.*, 2001] that is virtually identical in overall design to MAS but with an emphasis on matching many of the ASTER satellite bands. As a consequence, it lacks bands in the far infrared (CO_2 slicing bands) of use for cloud top altitude determination, especially for optically thin cirrus clouds. Table 2 summarizes the band center and bandwidth characteristics as well as main purpose of each MASTER band used for cloud retrievals during TC^4. The MASTER instrument acquired data for 6 research flights between 29 July and 8 August for a total of

27.5 hours of research data. The calibration of the infrared bands was obtained by viewing two onboard blackbodies each scan, as in the case of MAS.

Calibration of the shortwave bands is based on the same type of laboratory calibration as MAS; however, for TC[4], since this instrument was shipped down to San Jose, Costa Rica and integrated on the ER-2 aircraft as rapidly as possible, it had no pre-flight laboratory calibration available. Hence, in addition to a post-deployment laboratory calibration of the shortwave bands, comparisons were made between the radiometry of MASTER and collocated MODIS imagery in addition to a post-flight deployment over the ground calibration target of Railroad Valley, Nevada.

Comparison of the radiometry of MASTER and MODIS was achieved via examination of two coordinated overpasses with the Terra/MODIS over marine stratocumulus clouds on 29 July and 6 August 2007. The MASTER track was aligned directly with the MODIS track, such that the satellite was directly overhead at the time of the overpass. Using a carefully selected region of MASTER data (near nadir and within ±5 minutes of the overpass time) and data from the corresponding region of MODIS data, reflectance histograms for five wavelength bands were generated. Using this histogram analysis, MASTER data were then scaled to best match the MODIS data. An example of this analysis is shown in Figure 1 for the 0.87 μm band comparison from the 29 July 2007 overpass. The solid line is the MODIS data, the dotted line the MASTER data with no adjustment, and the dashed line the MASTER data with a 0.85 scale factor applied. Scale factors for all five bands, for both the 29 July and 6 August overpasses are provided in Table 3. Note that in Table 3, the adjustment of the MASTER 0.87 and 2.08 μm bands is based on histogram comparison of the retrieved cloud optical thickness and effective radius, respectively. For the 0.87 μm band, comparison based on the cloud optical thickness retrieval is nearly identical to that from the reflectance comparison, but for the 2.08 μm band, bandpass differences between MASTER and MODIS are appreciable enough that the effective radius retrievals provide a better comparison tool. Thus, based on the data in Table 3, the MASTER calibration used during TC^4 was reduced by 14% at 0.87 μm and 15% at 2.08 μm.

Since the MODIS/MASTER comparisons are limited to the six bands shown in Table 3, it is useful to examine the coordinated MASTER, MODIS, and surface reflectance measurements collected on 18 August 2007 over the Railroad Valley vicarious calibration site. Concurrent with the aircraft and satellite overpass, surface radiance measurements over the range of the MASTER shortwave bands were collected and processed using MODTRAN atmospheric correction to compute the radiance value expected at the aircraft flight level in a manner similar to that described by *Hook et al*. [2001]. After the appropriate MASTER pixels were identified (by locating ground tarps in the MASTER imagery) and averaged for each band, the ratio of the 'predicted' radiance to the measured (MASTER) radiance for all visible–SWIR bands except those in strong water vapor absorption regions was computed. Figure 2 shows this ratio as a function of wavelength for the 18 August overpass. Also included in Figure 2 are the MODIS/MASTER ratios (from comparative histogram analysis) that provides best agreement of MASTER with MODIS. The shortest wavelengths agree best, with some increase in disagreement for the longer wavelengths.

3. Cloud Retrievals

To retrieve cloud optical and microphysical properties, one must first evaluate the probability of a pixel being cloud contaminated, then determine its thermodynamic phase, and finally derive the cloud optical, microphysical, and physical properties (such as cloud optical thickness, effective radius, cloud top pressure, cloud top temperature, etc.). The previous version of our algorithm, described in *King et al*. [2004], discussed each of these steps in detail, with particular emphasis on retrievals over snow and sea ice surfaces. Therefore, the focus of this section will be on how our current algorithm, which is based closely on the MODIS Collection 5 retrieval algorithm, differs from our previous version, particularly as it pertains to retrievals over daytime ocean and land surfaces.

3.1. Cloud mask

The first decision on whether or not to derive cloud properties for a given pixel is to first determine the confidence that a pixel is obstructed by clouds. *King et al*. [2004] describe the basic logic of that procedure for the MAS cloud mask algorithm. The logic of the cloud mask algorithm we employed for TC^4 is quite similar, but with some modifications. Some of the alterations pertain to conditions encountered during TC^4, which was conducted largely over ocean, and to a lesser extent land, surfaces.

The nature of the ocean surface allows for more cloud mask tests to be performed than for any of the other four ecosystems (land, snow/ice, coastal, and desert). However, one factor that complicates the cloud mask tests over ocean is sunglint. Because sunglint can be so highly reflective, some cloud mask tests falsely identify sunglint as cloud. On other occasions, thin cloud such as cirrus can actually be masked by sunglint and thereby go undetected. Thus, to better process sunglint affected data, three notable improvements to the MAS/MASTER alborithm have been made to the cloud mask: (i) view angle dependent thresholds for the visible reflectance (0.87 μm) test in geometrically identified sunglint regions have been modified, (ii) a clear sky restoral test has been added that restores a pixel to clear sky if either the ratio of the 0.90 and 0.95 μm bands exceeds a threshold or the product of the mean and standard deviation of a region of 0.87 μm pixels exceeds a threshold (note however this clear sky restoral test is only invoked when no thermal test indicates cloud and the 3.7-11 μm brightness temperature difference exceeds a specified threshold), and (iii) comparison of the difference in Reynolds sea surface temperature (SST) and 11 μm brightness temperature to a threshold. Note this third test, which helps to improve identification of thin cirrus and low cloud in sunglint regions, is applied to the cloud probability computation of all water-processed pixels.

Three modifications were also made to cloud mask processing over land. These modifications include: (i) introduction of limited application of the simple 11 μm brightness temperature threshold test (previously used only over ocean), (ii) reduction of the threshold of the 3.9–11 μm (low cloud detection) brightness temperature difference test, and (iii) minor reduction of the visible reflectance thresholds. Additional details as well as thresholds for each test can be found in the MODIS cloud mask Algorithm Theoretical Basis Document [*Ackerman et al*., 2006] that is discussed and summarized in *Frey et al.* [2008].

3.2. Thermodynamic Phase

Knowledge of the cloud thermodynamic phase is critical to properly processing the cloud optical and microphysical properties. Thus we have developed a "decision tree" phase determination algorithm that is applied to each pixel identified by the cloud mask as cloudy or probably cloudy. The logic structure of the phase decision tree is similar for each of the five underlying ecosystems (land, ocean, snow/ice, coastal, and desert), but some minor differences (most notably thresholds) exist between the different ecosystems. *King et al*. [2004] describe the decision tree employed in our previous retrieval algorithm for the snow/ice ecosystem. Here we outline the thermodynamic phase decision tree currently employed in MODIS Collection 5 and applied to MAS and MASTER processing during TC^4.

Figure 3 shows the cloud mask tests and subsequent tests that are applied to pixels over ocean to determine whether the cloudy pixel contains liquid water cloud, ice cloud, or clouds of undetermined phase. In contrast to our earlier version, the 1.88 μm reflectance threshold test for ice cloud (1.88 μm reflectance $<$ 0.035) is no longer part of the initial phase decision, but now is only employed if no phase decision (undecided) results from both the initial phase tests, and after application of the infrared (IR) bispectral phase test described by *Baum et al*. [2000] and *King et al*. [2004]. This 1.88 μm test was moved to reduce the number of false ice cloud pixels found when a dry atmosphere exists above low level water cloud, as is a common occurrence over marine stratocumulus clouds over the subtropical ocean.

A second significant change from our earlier algorithm is that shortwave infrared (SWIR) tests are now implemented only if the reflectance of the nonabsorbing channel (0.87 μm over ocean and coastal surfaces) is greater than the surface albedo + 0.15. This avoids applying the SWIR ratio test to low reflectance clouds where ratios can be skewed either by a disproportionate influence of the underlying surface reflectance and/or the reflectance measurement uncertainty approaches the cloud reflectance value. A third difference in our current algorithm is that the thresholds of the liquid water cloud SWIR ratio tests are now dependent on the reflectance of a nonabsorbing band (a different threshold is used for “more visibly reflective” clouds—reflectance $>$ 0.5), as shown in detail in Figure 4. A final change to note from our previous version is the addition of a “warm sanity” check invoked after the SWIR tests (cf. Figure 3) that forces a pixel to liquid water cloud if the cloud top temperature is greater than 273 K.

3.3. Optical Properties of Liquid Water and Ice Clouds

After the cloud mask and thermodynamic phase estimation has been performed, the physical and optical properties of clouds can be retrieved using the physical principles first described by *Nakajima and King* [1990] and amplified by *Platnick et al*. [2003] and *King et al*. [2003] for MODIS observations. In the generation of the forward lookup library for ice clouds, new ice crystal size and habit distributions were used to generate an improved ice reflectance library. These microphysical models, described by *Baum et al.* [2005a], are based on 1100 size distributions analyzed from field campaigns in the midlatitudes, tropics, and subtropics, and characterize the size distributions in 45 size bins. The sizes (measured along the maximum dimension of the crystals) range from 2 to 9500 μm, while the shapes vary from droxals, bullet rosettes, hollow columns, solid columns, plates, and aggregates (cf. Fig. 5). Incorporating these size distributions and habit distributions into light scattering calculations [*Baum et al*., 2005b] results in reflectance libraries that typically lead to a reduction in effective radius of ice clouds in comparison to the previous collection 4 libraries described in *King et al.* [2004]. New light scattering calculations have been performed for the spectral bandwidth and location of both MASTER and MAS for use in airborne field campaigns, such as TC^4.

For our computations, we used the complex refractive indices of ice reported by *Gosse et al*. [1995] for wavelengths greater than 1.4 μm, which deviate from data published by *Warren* [1984] by as much as 60% at some wavelengths. We use Warren's compilation for wavelengths below 1.4 μm. For liquid water clouds, we have chosen to use the optical constants tabulated by Hale and *Querry* [1973] for bands below 0.872 μm, *Palmer and Williams* [1974] for the 1.618 μm band, and *Downing and Williams* [1975] for the 2.133 μm and greater bands.

3.4. Retrieval of Cloud Optical Thickness and Effective Radius

The simultaneous retrieval of cloud optical thickness and effective radius is best achieved by simultaneously measuring the reflection function at a visible and a near-infrared wavelength, and comparing the resulting measurements with theoretical calculations, as described by *Nakajima and King* [1990]. This technique is especially accurate over dark ocean surfaces because the reflection function of the earth–atmosphere system arises primarily from light scattering by the cloud layer, with little influence from the underlying surface. In comparing measurements with theory, however, it is essential that the light-scattering properties of the cloud are modeled realistically, and that the cloud is properly ascribed to either a liquid water cloud or an ice cloud with corresponding optical properties. For applications of this technique to land surfaces and surfaces containing snow or sea ice, it is vital to have an estimate of the underlying surface reflectance at appropriate visible and near-infrared wavelengths.

For MODIS Collection 5, and by extension MAS and MASTER retrievals from the NASA ER-2 aircraft, we utilized the spatially complete high-resolution snow-free surface albedo dataset first described by *Moody et al*. [2005]. This dataset was created by employing an ecosystem-dependant temporal interpolation technique to fill missing or seasonally snow-covered data in the operational MODIS Terra land surface product (MOD43B3). An aggregation using 5 years (2000-2004) of MOD43B3 data was used for the final Collection 5 production [*Moody et al*., 2008]. This dataset is stored in equal-angle grids for ease-of-use and has high temporal (16 day) and spatial (2 km) resolution for all MODIS, MAS, and MASTER bands of interest. Consequently, seasonal, spectral, and spatial variations of surface albedos are now more accurately represented. Further enhancements for treating snow-covered surfaces were incorporated into MODIS global processing, but this was unnecessary for any flights during TC^4.

For all MAS and MASTER cloud analysis during TC^4, we ported the operational cloud optical and microphysical properties algorithm from MODIS to MAS and MASTER, with instrument specific modifications to the thermodynamic phase algorithm as outlined previously. In addition to the surface albedo considerations over land surfaces, we have incorporated a clear sky restoral algorithm that attempts to identify pixels that are poor retrieval candidates, such as dust, smoke and sunglint, that are falsely identified as cloud by the cloud mask, and edge pixels not suitable for plane-parallel radiative transfer theory and its application. We have also implemented an algorithm to identify multi-layer clouds that is described in further detail in *Wind et al*. [2010]. This algorithm can be adapted more readily to MAS processing than MASTER due to the CO_2-slicing bands that exist on MAS.

This adaptation of MODIS-like processing to airborne MAS and MASTER sensors is unique, because the algorithm developed for satellite processing includes quality assurance and confidence flags, and uncertainty estimates for the cloud optical thickness and effective radius retrievals, most unusual for any airborne (and most satellite) analyses.

4. Results from Observations

During TC^4, the ER-2 acquired 41 h of MAS and/or MASTER data during 9 research flights between 17 July and 8 August 2007. These missions included coordinated measurements above, within, and below cirrus clouds to study the tropical tropopause transition layer (6 flights), and above and within liquid water and ice clouds in coordination with Terra satellite observations (4 flights) [*Toon et al*., 2010]. In what follows, we will describe results obtained from the ER-2 on two of these flights that were well coordinated with Terra observations, demonstrating the performance of the liquid water cloud optical property retrievals over ocean surfaces during the day, and comparisons of these airborne retrievals with nearly simultaneous observations from both MODIS and MISR onboard the Terra satellite.

4.1. Marine Stratocumulus off the Coast of Ecuador (29 July)

On 29 July, the ER-2 flew south over the Pacific to a region of extensive marine stratocumulus clouds off the coasts of Peru and Ecuador. At 1540 UTC the ER-2 turned NNE on a heading of 17.12° where it flew a flight leg of approximately 550 km in length (subdivided into flight lines 10 and 11 for convenience of data processing), in perfect alignment with a descending orbit of the Terra spacecraft that overflew the same ground track and extensive cloud field at 1557 UTC. This flight was useful for remote sensing of cloud radiative and microphysical properties over the ocean. Figure 6 shows the ER-2 ground track for this mission as divided into flight lines of the MASTER instrument for data processing.

Figure 7 shows a false-color composite image of flight line 10, together with images of cloud optical thickness (at 0.66 μm), cloud effective radius, and integrated water path. This scene consists of marine stratocumulus clouds 329 km in length over the eastern Pacific Ocean some 100 km west of the coast of Ecuador near Guayaquil Bay, where the ER-2 is flying from bottom (south) to top (north) up these images. The false-color image was constructed by contrast stretching and combining three spectral bands into one 24-bit image, where the spectral bands were assigned to red, green, and blue (RGB) 8-bit display channels. For this scene, the RGB assignment was 2.17 (red), 1.61 (green), and 0.66 μm (blue), and the scene consists entirely of boundary layer liquid water clouds, as determined by the cloud thermodynamic phase algorithm described earlier.

Having identified the corresponding scene as liquid water, we performed cloud optical property retrievals on average radiances from 5 × 5 pixel boxes as described in section 3.4. The second and third panel of Figure 7 shows retrievals of cloud optical thickness and effective radius derived using the retrieval algorithm adapted from the MODIS Collection 5 code for the solar and viewing geometries appropriate to this scene, where we regenerated the radiative transfer lookup tables for the spectral bands appropriate for MASTER (both liquid water and ice clouds, though this scene contains no ice clouds). The brighter liquid water clouds that appear white in the left-hand panel correspond to cloud optical thicknesses of 20 or more, whereas the browner and darker portions of the cloud yield an optical thickness closer to 6. The effective radius for this flight line is fairly uniform with values that range largely between 10 and 12 μm.

The right-hand panel of Figure 7 shows the cloud liquid water path W_c, which is derived from the product of cloud optical thickness τ_c and effective radius r_e as

$$W_c = 4/(3Q_e(r_e))\,\tau_c\, r_e, \tag{1}$$

where Q_e is the extinction efficiency at the same wavelength used to report the optical thickness retrieval (0.66 μm), and is a function of r_e. It has a value ≈2.

Figures 8a and 8b show the MASTER derived cloud optical thickness and effective radius for a combination of flight lines 10 and 11 along the coast of Ecuador, mapped onto geographic coordinates. Figures 8c and 8d show the corresponding retrievals from the Terra/MODIS observations for this portion of the eastern Pacific on 29 July. The larger geographic extent of the MODIS analysis allows one to see the expanse of the marine stratocumulus clouds and periodic breaks in the cloud field, but the MASTER results are inherently higher spatial resolution (50 m vs 1 km for MODIS).

In addition to porting the MODIS Collection 5 cloud optical property algorithm to work with MASTER, we also adapted the MODIS optical property retrieval to MISR data, since MISR was also available on the Terra spacecraft. Since MISR does not contain shortwave infrared channels necessary to derive cloud effective radius and identify the cloud's thermodynamic phase, we assumed these clouds were composed of liquid water having droplets with an effective radius of 10 μm. MISR optical thickness retrievals were made using the nadir camera. A recent MISR-MODIS study on this cloud type suggested minimal optical thickness retrieval variation across view angle cameras [*Liang et al.*, 2009]. We also derived the cloud top altitude from use of stereo but without allowing for the cloud-tracked winds that are routinely used in the MISR operational product. Figure 9 shows the results of this analysis, where Figure 9a is the retrieved cloud optical thickness and Figure 9b the cloud top altitude. The cloud top altitude derived from MISR is in close agreement with that derived from the Cloud Physics Lidar (CPL) onboard the ER-2 aircraft, which only provides cloud top altitude along the nadir track of the aircraft.

A numerical comparison of the various retrieval algorithms can best be seen by examining histograms of retrieved optical properties for the section of marine stratocumulus clouds observed by Terra and MASTER. Figure 10a shows comparisons of the probability density function of cloud optical thickness for all liquid water clouds contained within the MASTER flight lines 10 and 11 as derived by MODIS, MISR, and MASTER, with Fig. 13b showing the corresponding probability density of effective radius for MODIS and MASTER. As is commonly observed in global processing of MODIS cloud optical thickness, the distribution is highly skewed with fewer optically thick clouds. Both satellite instruments and MASTER show that the mode cloud optical thickness for these marine stratocumulus clouds is between 6 and 8, but with some clouds having an optical thickness up to about 50. Both MASTER and MODIS show the cloud effective radius falling largely between 8 and 13 μm, with the most between 10 and 12 μm.

4.2. Stratus Clouds in the Eastern Pacific off the Galapagos Islands (6 August)

On 8 August, the ER-2 flew southwest over the Pacific en route to the Galapagos Islands and the surrounding region of extensive marine stratocumulus. At 1633 UTC the ER-2 turned NNE on a heading of 16.25° where it flew a flight leg of approximately 264 km in length (flight line 14), in perfect alignment with a descending orbit of the Terra spacecraft that overflew the same ground track at 1645 UTC. Figure 6 shows the ER-2 ground track for this mission as divided into flight lines of the MASTER instrument.

Figure 11 shows a false-color composite image of flight line 14, together with images of cloud optical thickness, cloud effective radius, and integrated water path. This scene consists of clouds 329 km in length over the eastern Pacific Ocean some 1400 km southwest of San José, Costa Rica, and 300 km northwest of Isabela Island, Galapagos, where the ER-2 is flying from bottom (south) to top (north) up these images. The false-color image was constructed as in Figure 7, and the scene consists entirely of boundary layer liquid water clouds, as determined by the cloud thermodynamic phase algorithm described earlier. Based on the CPL onboard the ER-2, however, it was apparent that there was a very thin subvisible cirrus layer at 15 km altitude that was undetected in the passive imager data from the MASTER instrument.

The cloud system shown in Figure 11 was determined to be largely composed of liquid water clouds, and the multilayer cloud detection algorithm described by *Wind et al*. [2010] did not detect any subvisible cirrus clouds. The second and third panel of Figure 7 shows retrievals of cloud optical thickness and effective radius derived using our MODIS-adapted cloud retrieval algorithm. In Collection 5 we allowed ‘partial retrievals’ whereby a cloud optical thickness would be retrieved even when the optical thickness was too low to have any sensitivity to effective radius. This is apparent in the second and third panels of

Figure 11, where there were optical thickness retrievals in optically thin cloud for which there was no effective radius estimate. Edge pixel near holes in clouds are removed from the analysis in Collection 5 to decrease the impact of light scattering from 'broken' clouds, and this was also done in this case. Nevertheless, there were τ_c retrievals in some instances for which there was no corresponding r_e retrieval. The right-hand panel of Figure 11 shows the cloud liquid water path W_c derived from the product of cloud optical thickness and effective radius and, as such, has no retrieval when there is no r_e retrieval reported.

Figures 12a and 12b show the MASTER derived cloud optical thickness and effective radius for a flight lines 14, mapped onto geographic coordinates, with Figures 12c and 12d showing the corresponding retrievals from the Terra/MODIS observations for this portion of the eastern Pacific on 8 August. The purple pixels in the larger MODIS analysis indicate the regions where ice cloud was identified in our thermodynamic phase algorithm and retrieved using the MODIS ice libraries discussed in section 3.3 and Figure 5.

The MISR analysis of cloud optical thickness and cloud top altitude for a portion of this Terra/MISR orbit is shown in Figure 13. The cloud top altitude of 1–1.5 km for these boundary layer stratus clouds is consistent with the ER-2's CPL measurements as well, though the CPL detected subvisible cirrus clouds at 15 km that were also undetected by MISR. Again, assuming these were liquid water clouds having an effective radius of 10 μm, the MISR-derived cloud optical thickness for this scene is shown in Figure 13a, and is largely consistent with the MODIS retrievals shown in Figure 12c.

Figure 14a shows comparisons of the probability density function of cloud optical thickness for all liquid water clouds contained within MASTER flight line 14 as derived by MODIS, MISR, and MASTER, with Fig. 14b showing the corresponding probability density of effective radius for MODIS and MASTER. This is the same scale as shown above for 29 July (Figure 10), from which it is obvious that the cloud optical thickness distribution is very similar to the clouds off the coast of Ecuador, but the effective radius of these clouds far off shore are much larger than those observed close to the coast. As seen previously, there is very good agreement between retrievals using MODIS, MASTER, and MISR for cloud optical thickness and between MODIS and MASTER for effective radius. Since the effective radius of these liquid water clouds ranges more between 16 and 20 μm, and 10 μm was assumed in the MISR retrievals of cloud optical thickness, some errors in MISR τ_c retrievals are to be expected.

5. Summary and Conclusions

High-resolution images of the spectral reflection function and thermal emission of the earth–atmosphere system were obtained with the MODIS Airborne Simulator (MAS) and MODIS/ASTER Airborne Simulator (MASTER) operated from the NASA ER-2 aircraft during the TC^4 experiment, conducted over Central America and the neighboring eastern Pacific Ocean and Caribbean Sea between 17 July and 8 August 2007. Multispectral images of the reflectance and brightness temperature at 11 (9) wavelengths between 0.66 and 13.98 (12.19) μm were used to derive the probability of clear sky (or cloud), cloud thermodynamic phase, and the optical thickness and effective radius of liquid water and ice clouds from MAS (MASTER).

In this paper, we compared retrievals of cloud optical thickness and effective radius from MASTER with a virtually identical algorithm used to process MODIS data on the Terra and Aqua spacecraft. This comparison was conducted for two well-coordinated flights of the ER-2 aircraft underneath the Terra spacecraft, both of which were over extensive marine stratocumulus clouds composed exclusively of liquid water droplets. In addition to comparisons between

MASTER and MODIS, we adapted the MODIS operational cloud retrieval code to work on MISR data acquired from the Terra spacecraft, but with the necessary assumptions about the cloud effective radius and thermodynamic phase, since MISR lacks the spectral bands that would permit this determination unambiguously. In both of these comparisons, the probability density functions of cloud optical thickness and effective radius were nearly identical, providing further confidence in the ability of MODIS to derive cloud optical properties over extensive liquid water clouds over the ocean, with very little impact of using a 1 km spatial resolution retrieval in comparison to the higher resolution of 50 m available from MASTER (and MAS) for these clouds. Some of the sophisticated algorithm features implemented in MODIS, such as clear-sky restoral to account for sun glint and false cloud detection, and cloud edge removal, were also adapted to MASTER (and MAS).

Throughout the TC^4 campaign, the best satellite coordination between the ER-2 and Terra occurred late in the deployment, when MASTER was used instead of MAS. In addition, the clouds that occurred during these intercomparison opportunities, and reported in this paper, were liquid water clouds over the eastern Pacific Ocean. Though there were no satellites with which to compare results during other flights of TC^4, the same algorithm for both MASTER and MAS that is described in this paper, and which is applicable for both liquid water and ice clouds, can be used to compare with other airborne and in situ measurements. With the algorithm described, MAS retrievals over ice clouds early in the campaign were used in studies reported in *Jensen et al*. [2009], *Eichler et al*. [2010, this issue], *Kindel et al*. [2010, this issue], and *Schmidt et al*. [2010, this issue].

Acknowledgments. The research reported in this article was supported by the MODIS Science Team and NASA's Radiation Sciences Program. MDK was supported by NASA Grant NNX08AR39G to the University of Colorado.

References

Ackerman, S., K. Strabala, P. Menzel, R. Frey, C. Moeller, L. Gumley, B. Baum, S. W. Seemann, and H. Zhang (2006), Discriminating clear-sky from cloud with MODIS algorithm theoretical basis document (MOD35), *Goddard Space Flight Center*, 125 pp. [Available online at modis-atmos.gsfc.nasa.gov/_docs/MOD35:MYD35_ATBD_C005.pdf].

Baum, B. A., P. F. Soulen, K. I. Strabala, M. D. King, S. A. Ackerman, W. P. Menzel, and P. Yang (2000), Remote sensing of cloud properties using MODIS Airborne Simulator imagery during SUCCESS. II: Cloud thermodynamic phase, *J. Geophys. Res.*, *105*, 11781-11792.

Baum, B. A., A. J. Heymsfield, P. Yang, and S. T. Bedka (2005a), Bulk scattering properties for the remote sensing of ice clouds. Part I: Microphysical data and models, *J. Appl. Meteor.*, *44*, 1885-1895.

Baum, B. A., P. Yang, A. J. Heymsfield, S. Platnick, M. D. King, Y. X. Hu, and S. T. Bedka (2005b), Bulk scattering properties for the remote sensing of ice clouds. Part II: Narrowband models, *J. Appl. Meteor.*, *44*, 1896-1911.

Downing, H. D., and D. Williams (1975), Optical constants of water in the infrared, *J. Geophys. Res.*, *80*, 1656-1661.

Eichler, H., K. S. Schmidt, R. Buras, M. Wendisch, B. Mayer, P. Pilewskie, M. D. King, L. Tian, G. Heymsfield, and S. Platnick (2010), Cirrus spatial heterogeneity versus ice crystal shape: Effects on remote sensing of cirrus optical thickness and effective crystal radius, Submitted to *J. Geophys. Res.*

Frey, R. A., S. A. Ackerman, Y. Liu, K. I. Strabala, H. Zhang, J. R. Key, and X. Wang (2008), Cloud detection with MODIS. Part I: Improvements in the MODIS cloud mask for collection 5, *J. Atmos. Oceanic Technol.*, *25*, 1057-1072.

Gosse, S., D. Labrie, and P. Chylek (1995), Refractive index of ice in the 1.4 to 7.8

μm spectral range, *Appl. Opt.*, *34*, 6582-6586.

Hale, G. M., and M. R. Querry (1973), Optical constants of water in the 200-nm to 200-μm wavelength region, *Appl. Opt.*, *12*, 555-563.

Hook, S. J., J. J. Myers, K. J. Thome, M. Fitzgerald, and A. B. Kahle (2001), The MODIS/ASTER airborne simulator (MASTER)—A new instrument for earth science studies, *Remote Sens. Environ.*, *76*, 93-102.

Jensen, E. J., P. Lawson, B. Baker, B. Pilson, Q. Mo, A. J. Heymsfield, A. Bansemer, T. P. Bui, M. McGill, D. Hlavka, G. Heymsfield, S. Platnick, G. T. Arnold, and S. Tanelli (2009), On the importance of small ice crystals in tropical anvil cirrus, *Atmos. Chem. Phys.*, *9*, 5519-5537.

Kindel, B. C., K. S. Schmidt, P. Pilewskie, B. Baum, P. Yang, and S. Platnick (2010), Observations and modeling of cirrus shortwave spectral albedo during the Tropical Composition, Cloud and Climate Coupling Experiment, submitted to *J. Geophys. Res*.

King, M. D., and D. D. Herring (2003), Monitoring Earth's vital signs, *Sci. Amer.*, *282*, 72-77.

King, M. D, W. P. Menzel, P. S. Grant, J. S. Myers, G. T. Arnold, S. E. Platnick, L. E. Gumley, S. C. Tsay, C. C. Moeller, M. Fitzgerald, K. S. Brown, and F. G. Osterwisch (1996), Airborne scanning spectrometer for remote sensing of cloud, aerosol, water vapor and surface properties, *J. Atmos. Oceanic Technol.*, *13*, 777-794.

King, M. D., S. Platnick, P. Yang, G. T. Arnold, M. A. Gray, J. C. Riedi, S. A. Ackerman, and K. N. Liou (2004), Remote sensing of liquid water and ice cloud optical thickness and effective radius in the arctic: Application of airborne multispectral MAS data, *J. Atmos. Oceanic Technol.*, *21*, 857-875.

King, M. D, W. P. Menzel, Y. J. Kaufman, D. Tanré, B. C. Gao, S. Platnick, S. A. Ackerman, L. A. Remer, R. Pincus, and P. A. Hubanks (2003), Cloud and aerosol properties, precipitable water, and profiles of temperature and humidity from MODIS, *IEEE Trans. Geosci. Remote Sens.*, *41*, 442-458.

Liang, L., L. Di Girolamo, and S. Platnick (2009), View-angle consistency in reflectance, optical depth, and spherical albedo of marine water clouds off the coast of California through MISR-MODIS fusion, *Geophys. Res. Lett.*, *36*, L09811, doi:10.1029/2008GL037124.

Moody, E. G., M. D. King, S., Platnick, C. B. Schaaf, and F. Gao (2005), Spatially complete global spectral surface albedos: Value-added datasets derived from Terra MODIS land products, *IEEE Trans. Geosci. Remote Sens.*, *43*, 144-158.

Moody, E. G., M. D. King, C. B. Schaaf, and S. Platnick (2008), MODIS-derived spatially complete surface albedo products: Spatial and temporal pixel distribution and zonal averages, *J. Appl. Meteor. Climatol.*, *47*, 2879-2894.

Nakajima, T., and M. D. King (1990), Determination of the optical thickness and effective particle radius of clouds from reflected solar radiation measurements, Part I: Theory, *J. Atmos. Sci.*, *47*, 1878-1893.

Palmer, K. F., and D. Williams (1974), Optical properties of water in the near infrared, *J. Opt. Soc. Amer.*, *64*, 1107-1110.

Parkinson, C. L. (2003), Aqua: An Earth-observing satellite mission to examine water and other climate variables, *IEEE Trans. Geosci. Remote Sens.*, *41*, 173-183.

Platnick, S., M. D. King, S. A. Ackerman, W. P. Menzel, B. A. Baum, J. C. Riedi, and R. A. Frey (2003), The MODIS cloud products: Algorithms and examples from Terra, *IEEE Trans. Geosci. Remote Sens.*, *41*, 459-473.

Schmidt, K. S., P. Pilewskie, B. Mayer, M. Wendisch. B. Kindel, S. Platnick, M. D. King, G. Wind, G. T. Arnold, L. Tian, G. Heymsfield, and H. Eichler (2010), Apparent and real absorption of solar spectral irradiance in heterogeneous ice clouds, Submitted to *J. Geophys. Res.*

Toon, O. B., D. O'C. Starr, E. Jensen, P. Newman, S. Platnick, M. Schoeberl, P. Wennberg, S. Wofsy, M. Kurylo, H. Maring, K. Jucks, M. Craig, M. Vasquez, L. Pfister, K. Rosenlof, H. Selkirk, P. Colarco, R. Kawa, J. Mace, P. Minnis, and K. Pickering (2010), Planning and implementation of the tropical composition, cloud and climate coupling experiment (TC^4), *J. Geophys. Res.*, submitted.

Warren, S. G. (1984), Optical constants of ice from the ultraviolet to the microwave, *Appl. Opt.*, *23*, 1206-1225.

Wind, G., S. Platnick, M. D. King, P. A. Hubanks, M. J. Pavolonis, A. K. Heidinger, P. Yang, and B. A. Baum (2010), Multilayer cloud detection with the MODIS near-infrared water vapor absorption band, Submitted to *J. Appl. Meteor. Climatol*.

TABLE 1. Spectral and radiometric characteristics of all MAS channels used in the cloud mask, cloud phase, and cloud optical property retrievals during TC^4 (daytime conditions).

MAS channel	Equivalent MODIS band	Central wavelength (μm)	Spectral resolution (μm)	Cloud Mask	Cloud Phase	Cloud Retrievals	Primary Purpose(s)
3	1	0.66	0.05	✓	✓	✓	Thick cloud; cloud optical thickness over land; cloud phase
7	2	0.87	0.04	✓	✓	✓	Thick cloud; cloud optical thickness over ocean; cloud phase
9	19	0.95	0.04		✓	✓	Cloud phase; multilayer cloud
10	6	1.61	0.05	✓	✓	✓	Cloud phase–SWIR ratio test; cloud effective radius
15		1.88	0.05	✓	✓	✓	Thin cirrus; cloud phase; clear sky restoral
20	7	2.13	0.05	✓	✓	✓	Cloud phase–SWIR ratio test; cloud effective radius
30	20	3.76	0.13	✓		✓	Cloud effective radius
31	21	3.92	0.15	✓	✓		Low thick cloud; cloud phase
42	29	8.55	0.40	✓	✓		Cloud phase
45	31	11.01	0.50	✓	✓	✓	Thin cirrus over ocean; cloud top properties
46	32	12.02	0.47	✓			Thin cirrus
48	33	13.26	0.43		✓	✓	Cloud phase; cloud top properties
49	35	13.80	0.55	✓	✓	✓	Mid-level clouds; cloud phase; cloud top properties

TABLE 2. Spectral and radiometric characteristics of all MASTER channels used in the cloud mask, cloud phase, and cloud optical property retrievals during TC^4 (daytime conditions).

MASTER channel	Equivalent MODIS band	Central wavelength (μm)	Spectral resolution (μm)	Cloud Mask	Cloud Phase	Cloud Retrievals	Primary Purpose(s)
5	1	0.66	0.06	✓	✓	✓	Thick cloud; cloud optical thickness over land; cloud phase
9	2	0.87	0.04	✓	✓	✓	Thick cloud; cloud optical thickness over ocean; cloud phase
11	19	0.95	0.04		✓	✓	Cloud phase; multilayer cloud; cloud top properties
12	6	1.61	0.06	✓	✓	✓	Cloud phase–SWIR ratio test; cloud effective radius
17		1.88	0.05	✓	✓	✓	Thin cirrus; cloud phase; clear sky restoral
20	7	2.08	0.05		✓	✓	Cloud phase–SWIR ratio test; cloud effective radius
30	20	3.73	0.14	✓		✓	Cloud effective radius
31	21	3.89	0.16	✓	✓		Low thick cloud; cloud phase
43	29	8.63	0.38	✓	✓		Cloud phase
47	31	10.68	0.61	✓	✓	✓	Thin cirrus over ocean; cloud top properties
49	32	12.19	0.52	✓			Thin cirrus

TABLE 3. Scale factors applied to MASTER to align radiometry with MODIS histograms.

	Central wavelength (μm)					
Date	0.46	0.54	0.66	0.87	1.61	2.08
29 July	1.04	0.88	0.87	0.86[a]	0.82	0.85[b]
6 August	1.06	0.89	0.87	0.86[a]	0.83	0.85[b]

[a]comparison based on retrieved optical thickness comparison
[b]comparison based on retrieved effective radius comparison

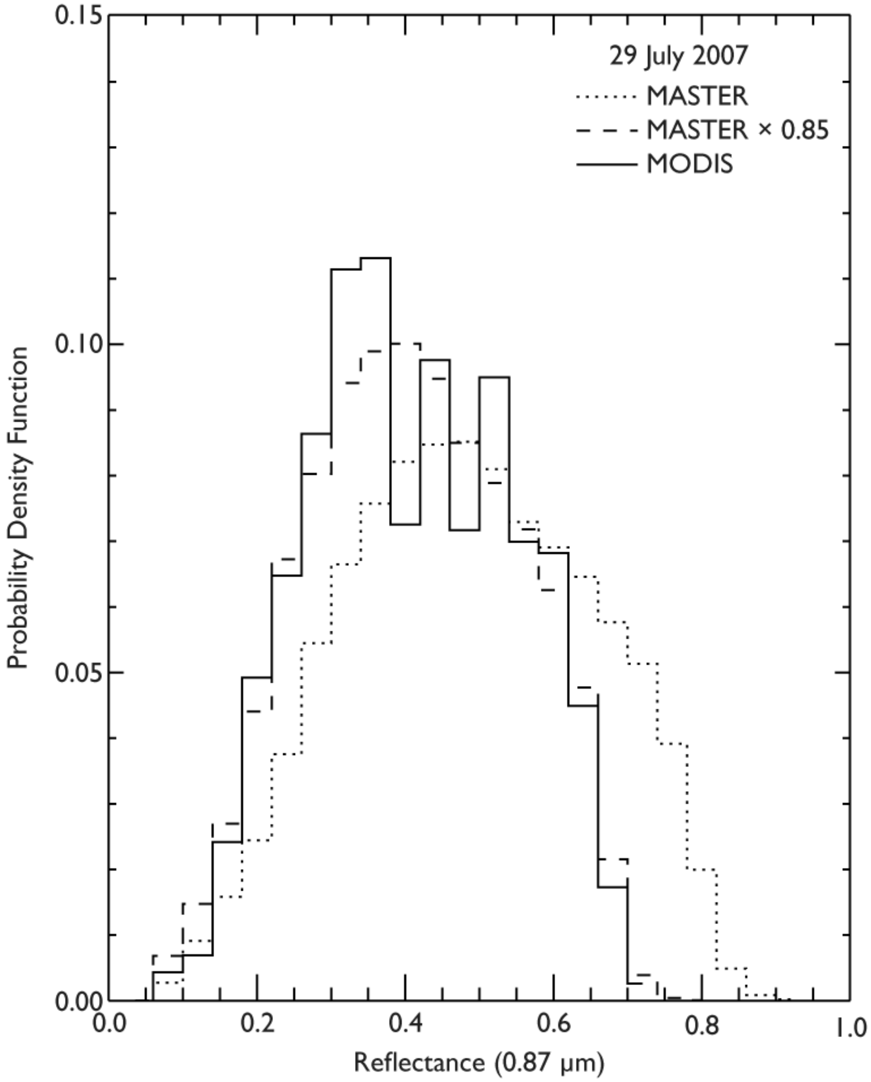

Figure 1. Histograms of Terra/MODIS reflectances at 0.87 μm over marine stratocumulus clouds on 29 July 2007. Comparable histograms of MASTER radiances before and after making calibration adjustments are shown for comparison. A 15% reduction in the pre-flight calibration at 0.87 μm was necessary to bring the MODIS and MASTER calibrations into close agreement.

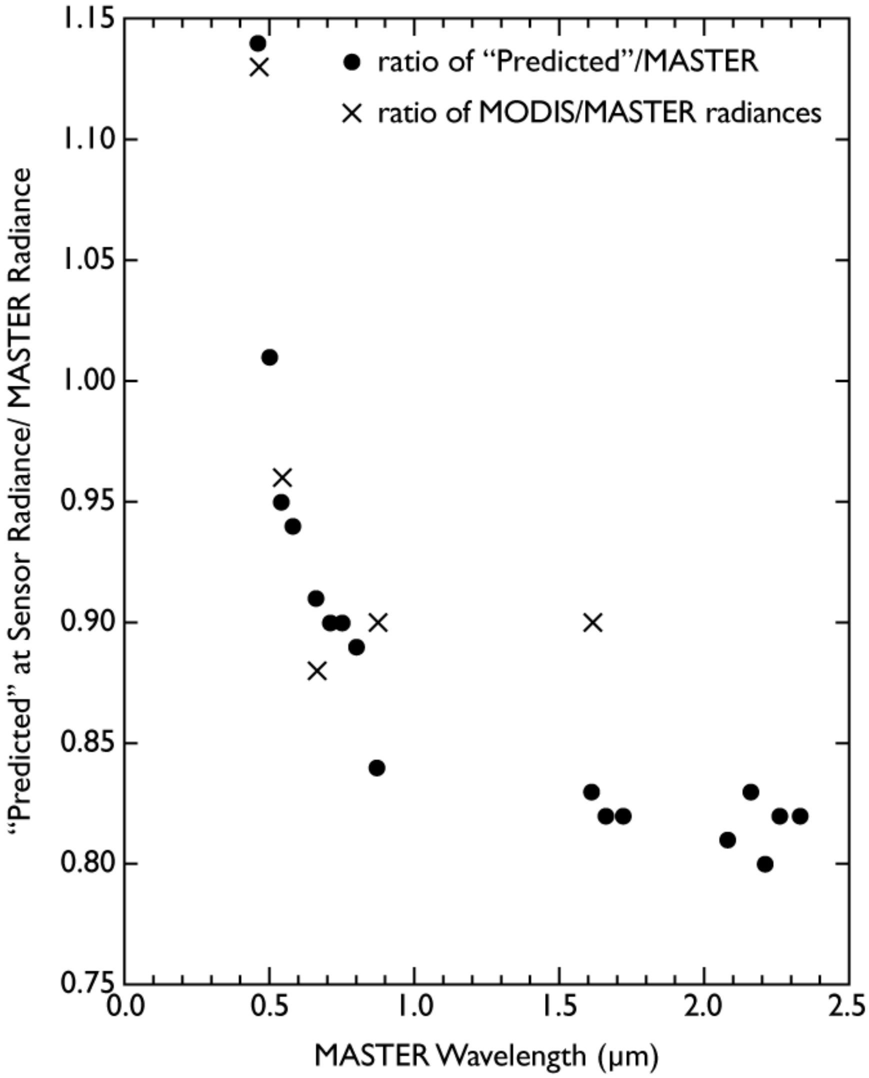

Figure 2. Ratio of predicted radiance at the MASTER sensor to that measured using pre-launch calibration on 18 August 2007 (solid circles) as a function of wavelength. The crosses indicate the ratio of the MODIS/MASTER radiances at comparable bands of MODIS and MASTER.

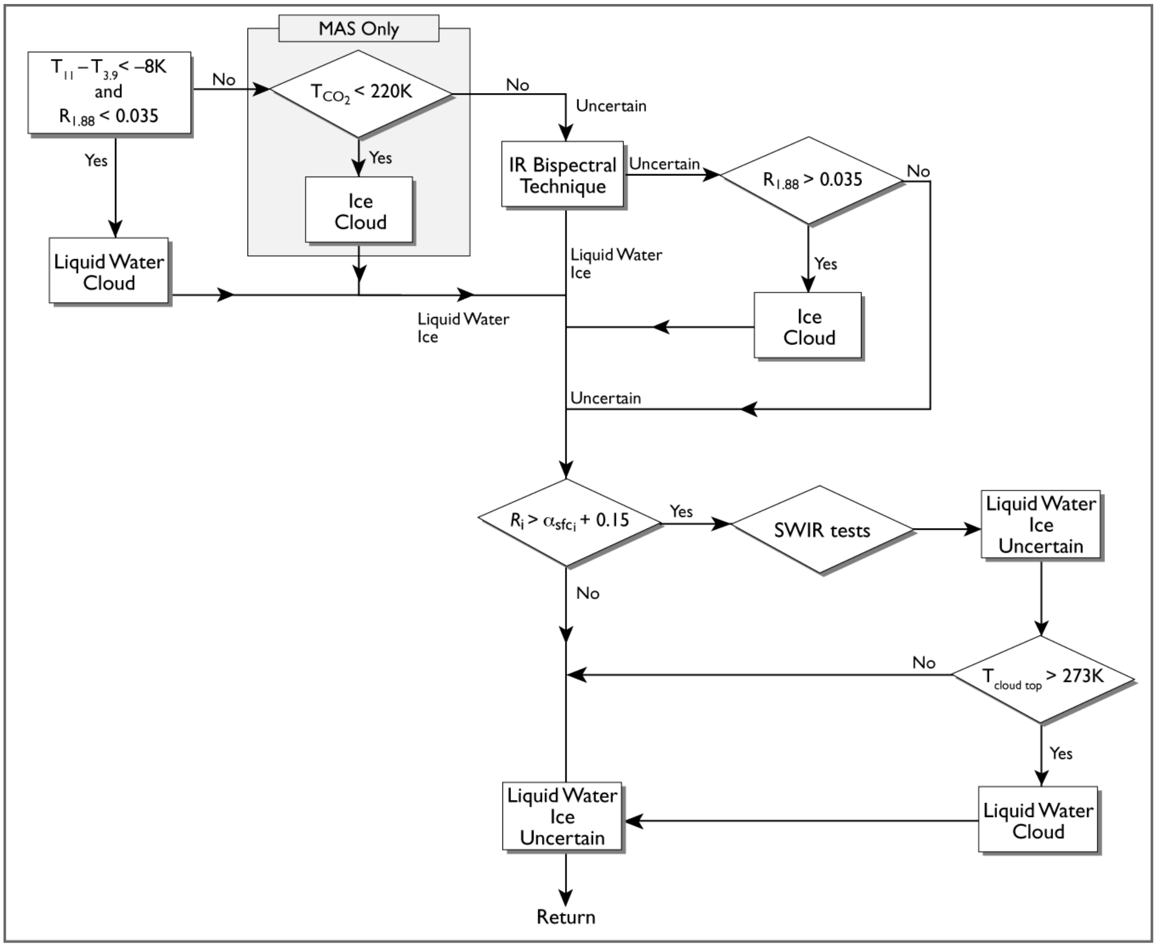

Figure 3. Flowchart for determining cloud thermodynamic phase over ocean during the daytime using MAS or MASTER.

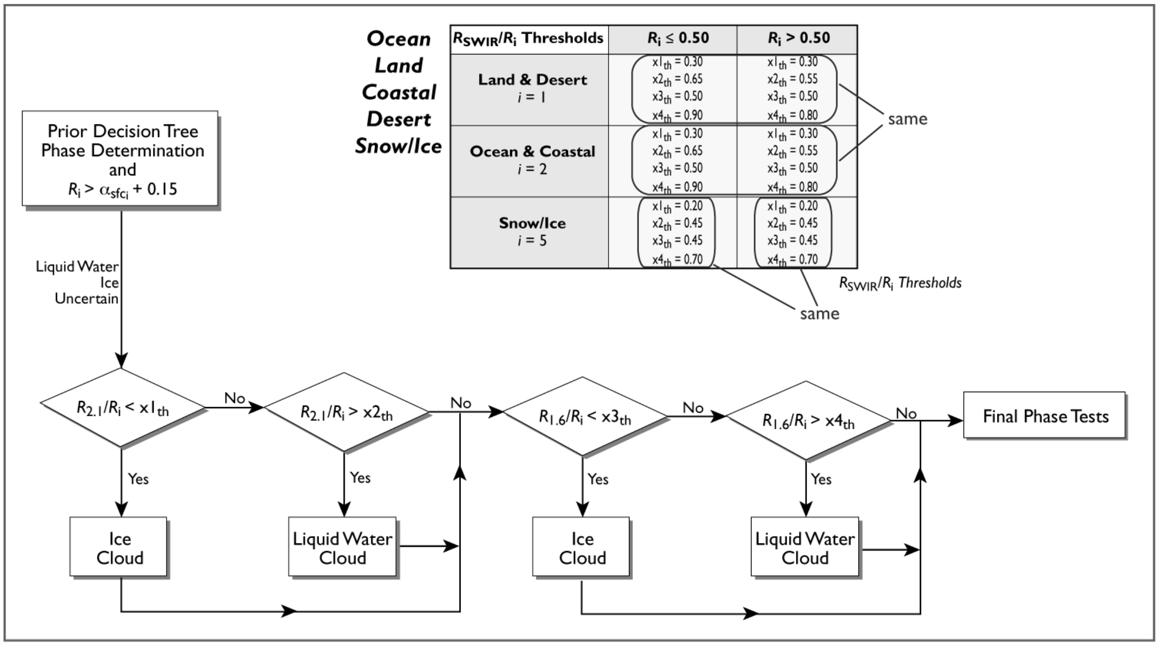

Figure 4. Flowchart showing the details of the shortwave infrared (SWIR) ratio tests used as part of the cloud thermodynamic phase algorithm.

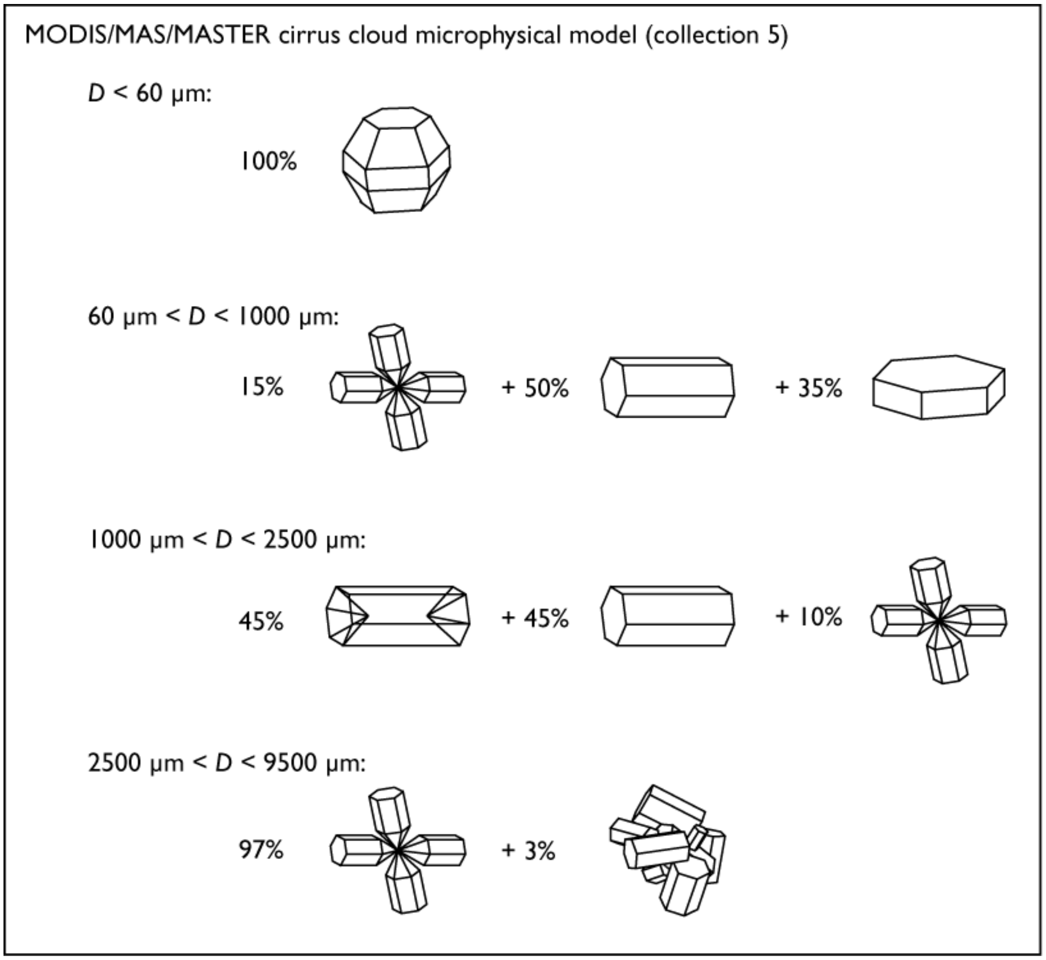

Figure 5. The distribution of ice crystal habit assumed in the microphysical model used for MODIS, MAS, and MASTER retrievals of cirrus cloud optical properties (Collection 5). Note that *D* is the maximum dimension of an ice crystal.

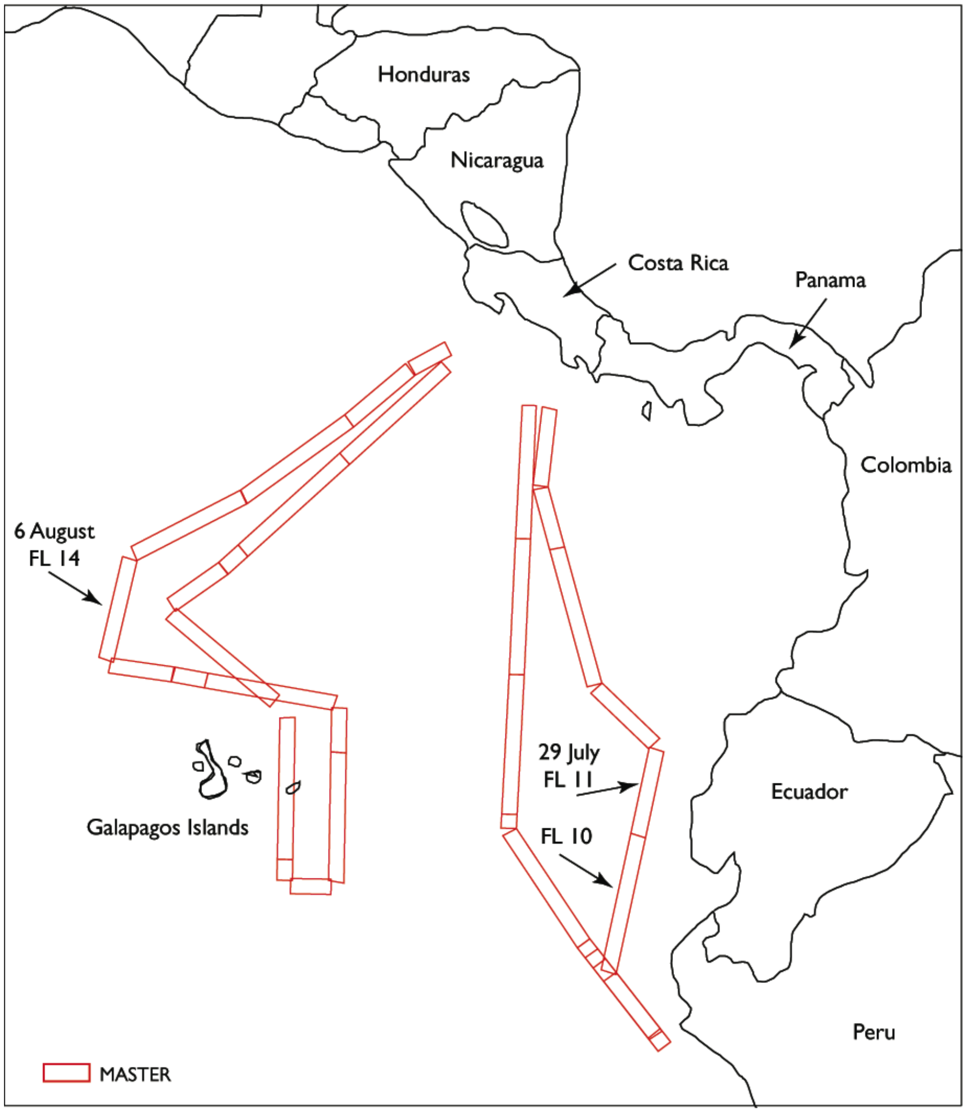

Figure 6. Ground track of the NASA ER-2 aircraft on 29 July and 6 August 2007.

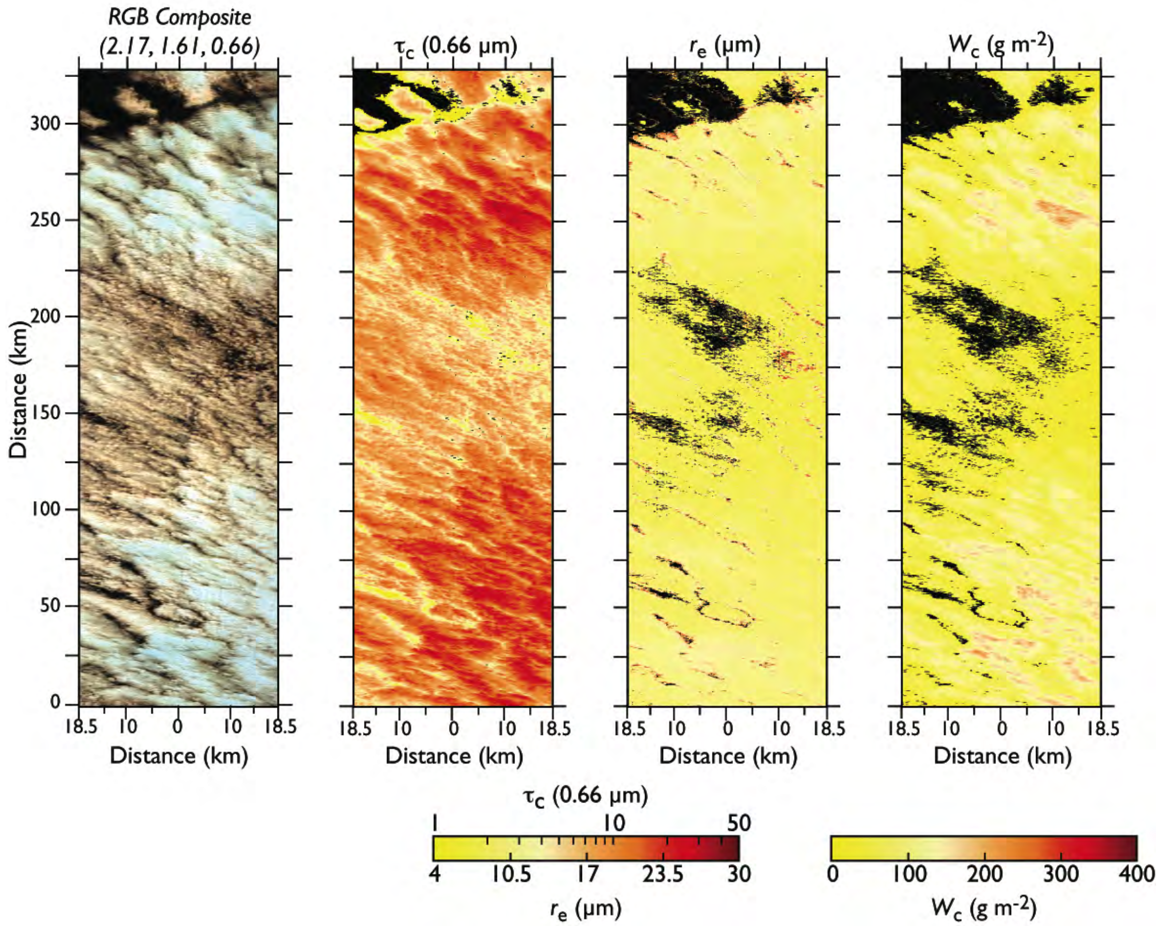

Figure 7. Composite MASTER image and derived cloud optical properties of marine stratocumulus clouds off Ecuador on 29 July 2007 (flight line 10). The first panel shows an RGB composite image with color assignment: red (2.17 μm), green (1.61 μm), and blue (0.66 μm). The second panel is the resultant cloud optical thickness, the third panel the effective radius, and the final panel the cloud integrated water path.

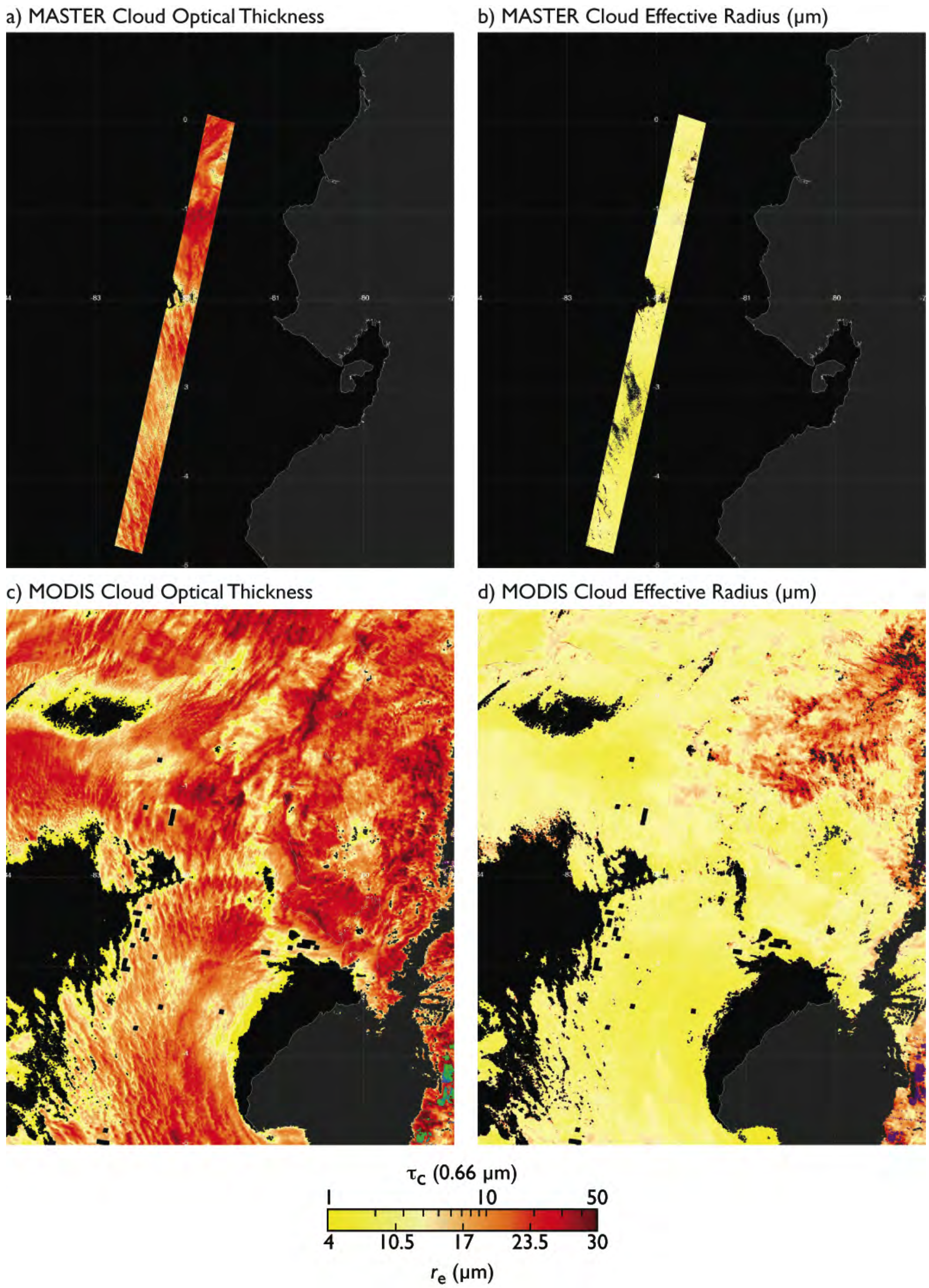

Figure 8. Cloud optical thickness and effective radius derived from MASTER and Terra/MODIS on 29 July 2007 of the coast of Ecuador. The pair of images on the left corresponds to optical thickness, and the pair of images on the right corresponds to the effective radius.

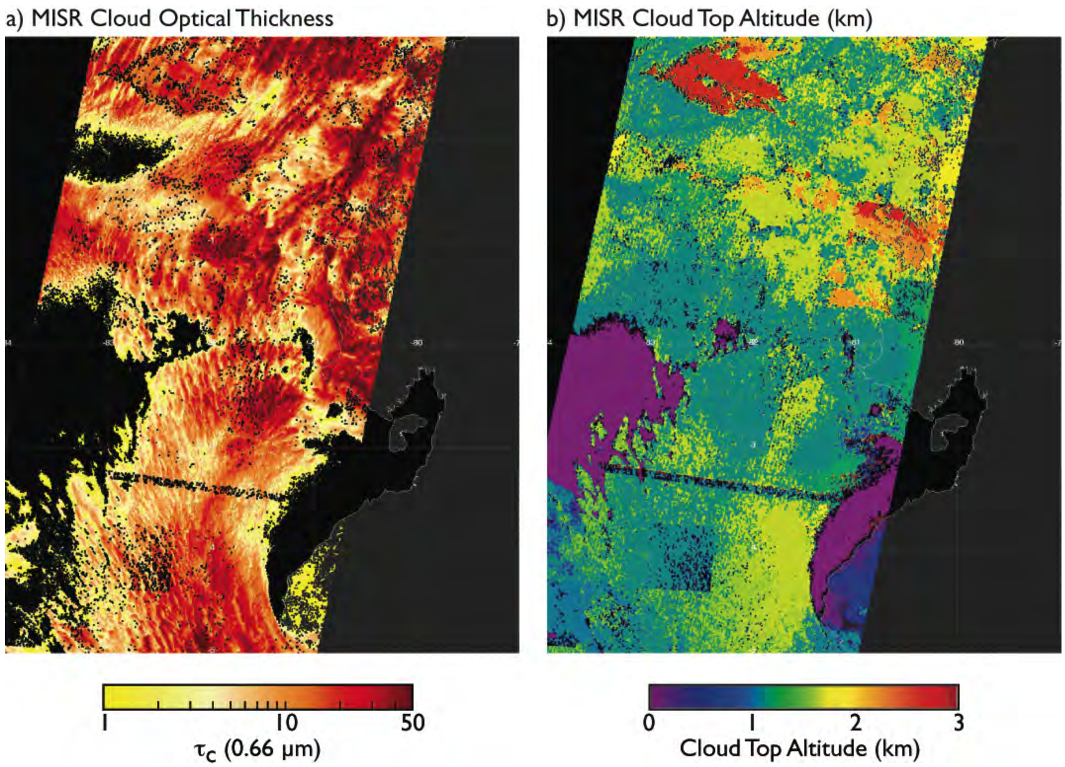

Figure 9. Cloud optical thickness and cloud top altitude retrieved from MISR on 29 July 2007 off the coast of Ecuador.

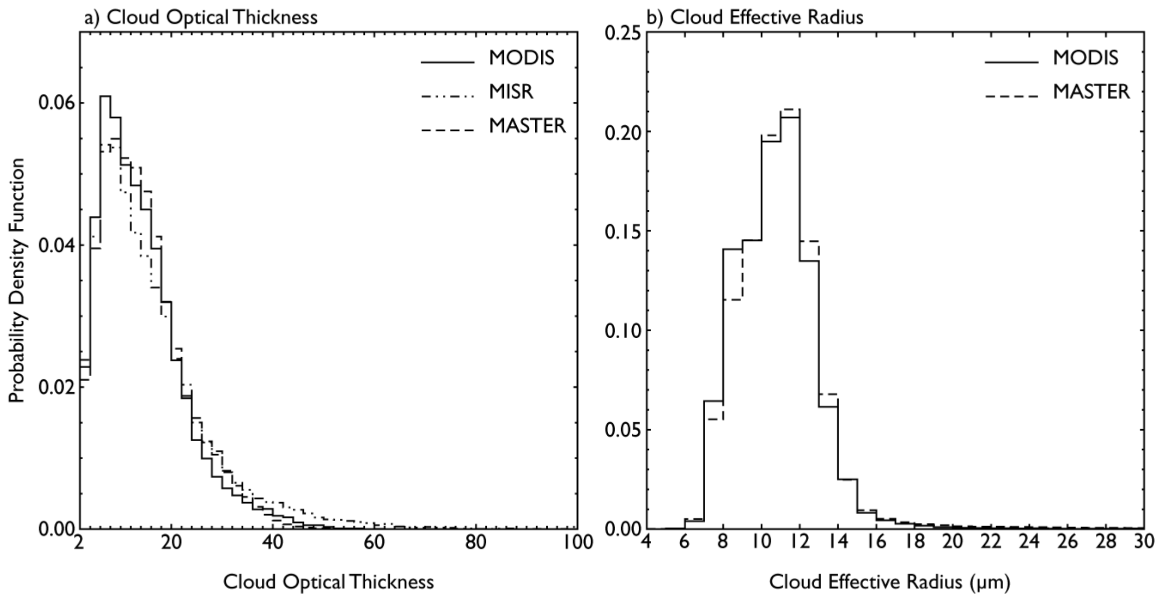

Figure 10. Marginal probability density function of cloud optical thickness and effective radius for all liquid water pixels in MASTER flight lines 10 and 11 on 29 July 2007 off the coast of Ecuador. Superimposed on these distributions are the probability distributions of cloud optical thickness derived from collocated MODIS and MISR observations in panel (a) and effective radius from MODIS in panel (b).

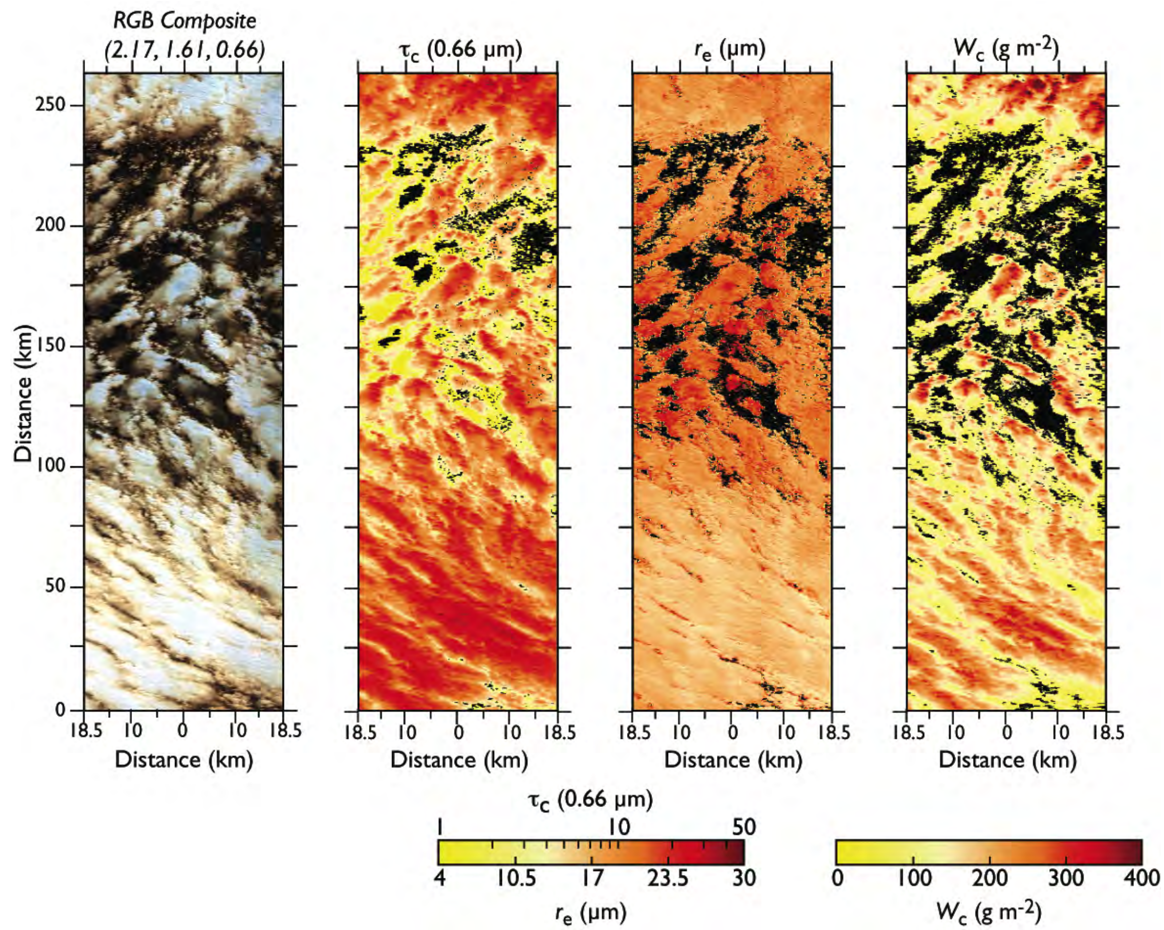

Figure 11. Composite MASTER image and derived cloud optical properties of marine stratocumulus clouds near the Galapagos Islands on 6 August 2007 (flight line 10). The first panel shows an RGB composite image with color assignment: red (2.17 μm), green (1.61 μm), and blue (0.66 μm). The second panel is the resultant cloud optical thickness, the third panel the effective radius, and the final panel the cloud integrated water path.

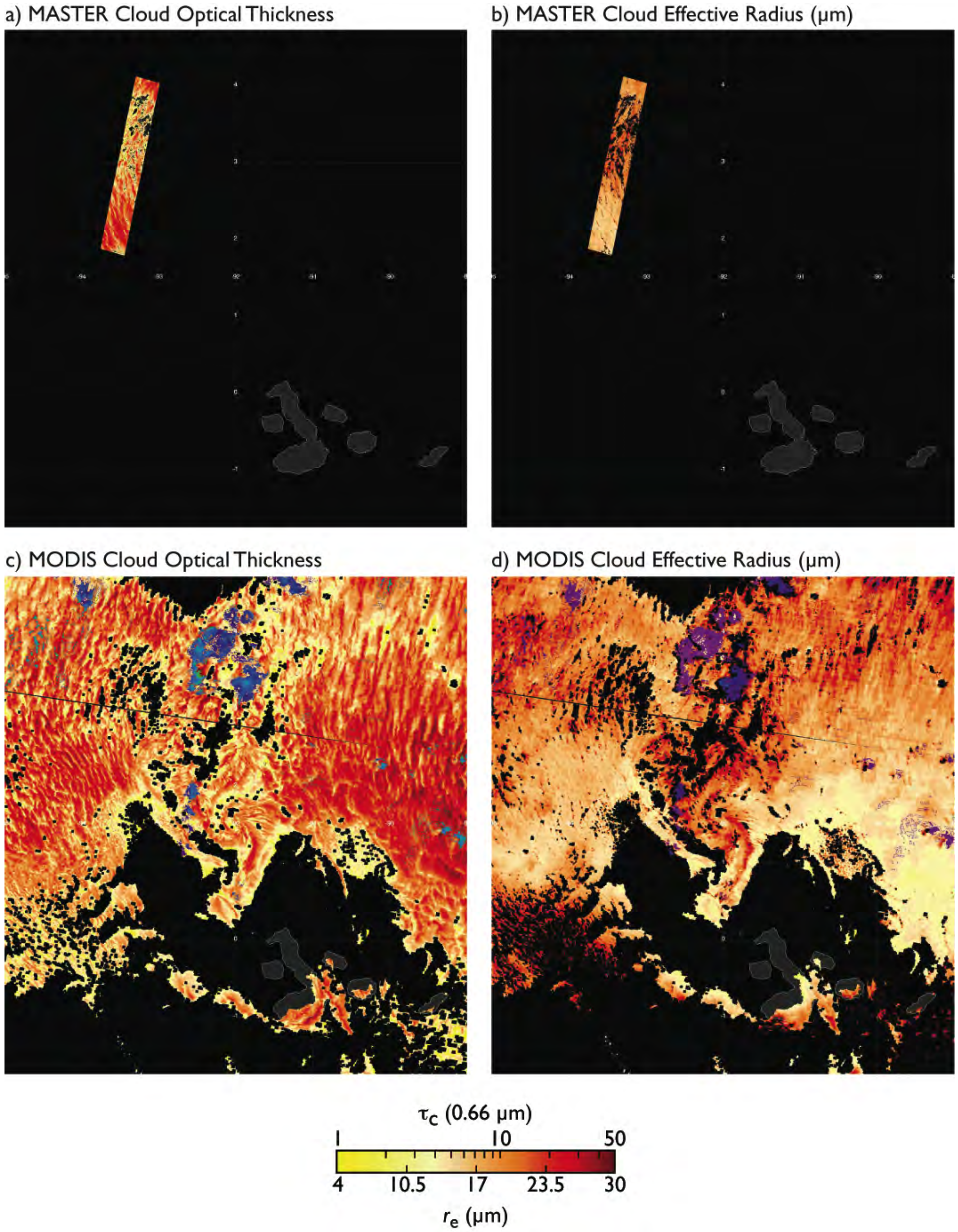

Figure 12. Cloud optical thickness and effective radius derived from MASTER and Terra/MODIS near the Galapagos Islands on 6 August 2007. The pair of images on the left corresponds to optical thickness, and the pair of images on the right corresponds to the effective radius.

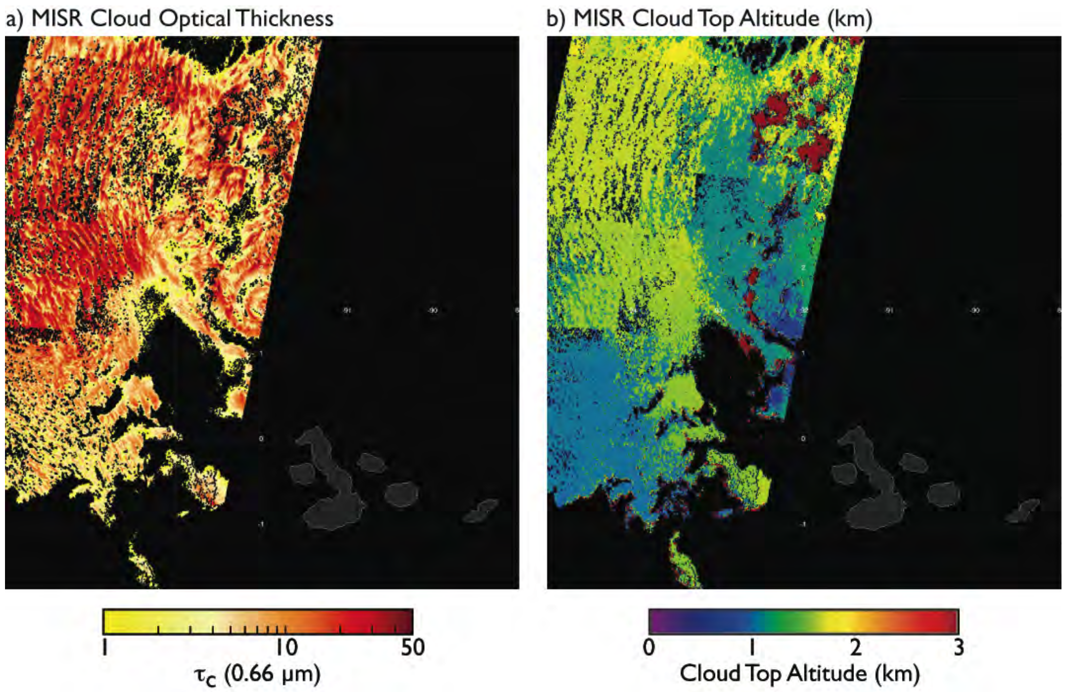

Figure 13. Cloud optical thickness and cloud top altitude retrieved from MISR on 6 August 2007 near the Galapagos Islands.

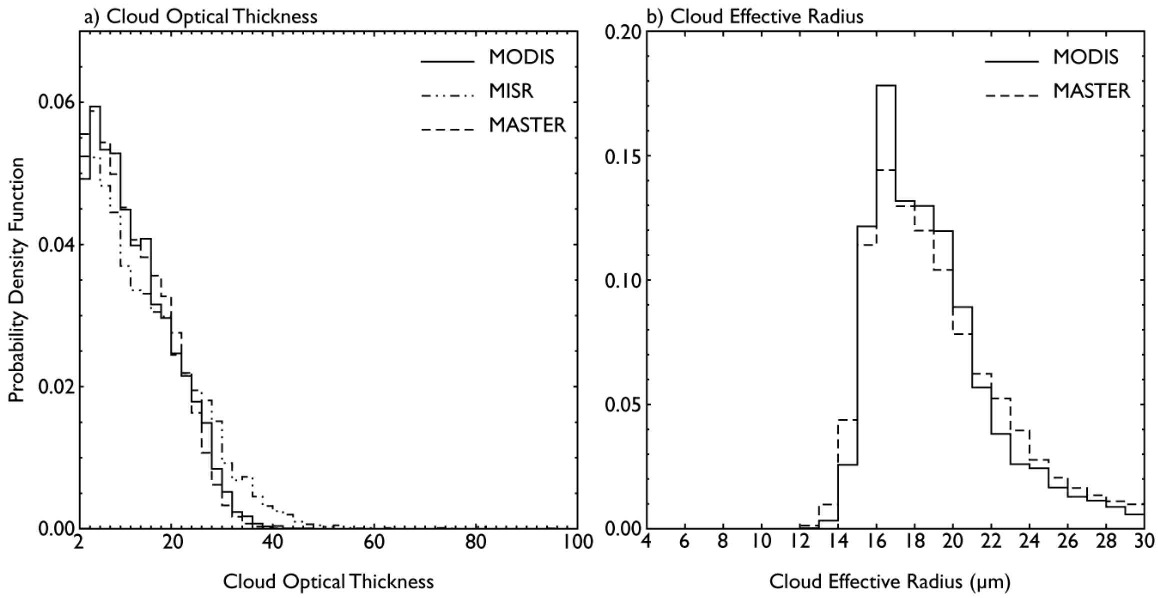

Figure 14. Marginal probability density function of cloud optical thickness and effective radius for all liquid water pixels in MASTER flight line 14 on 6 August 2007 northwest of the Galapagos Islands. Superimposed on these distributions are the probability distributions of cloud optical thickness derived from collocated MODIS and MISR observations in panel (a) and effective radius from MODIS in panel (b).